Picosecond amorphization of SiO₂ stishovite under tension

Masaaki Misawa,[1,2] Emina Ryuo,[2] Kimiko Yoshida,[3] Rajiv K. Kalia,[1] Aiichiro Nakano,[1]* Norimasa Nishiyama,[4] Fuyuki Shimojo,[2] Priya Vashishta,[1] Fumihiro Wakai[3]

It is extremely difficult to realize two conflicting properties—high hardness and toughness—in one material. Nano-polycrystalline stishovite, recently synthesized from Earth-abundant silica glass, proved to be a super-hard, ultra-tough material, which could provide sustainable supply of high-performance ceramics. Our quantum molecular dynamics simulations show that stishovite amorphizes rapidly on the order of picosecond under tension in front of a crack tip. We find a displacive amorphization mechanism that only involves short-distance collective motions of atoms, thereby facilitating the rapid transformation. The two-step amorphization pathway involves an intermediate state akin to experimentally suggested "high-density glass polymorphs" before eventually transforming to normal glass. The rapid amorphization can catch up with, screen, and self-heal a fast-moving crack. This new concept of fast amorphization toughening likely operates in other pressure-synthesized hard solids.

INTRODUCTION

Silica [silicon dioxide (SiO₂)] is the most abundant constituent of Earth's crust (1) and has many polymorphs. Under ambient conditions, each silicon atom in silica is surrounded by four oxygen atoms. In 1961, Stishov and Popova synthesized a high-pressure polymorph of silica, in which each silicon atom is six-coordinated (2). The same polymorph was later discovered in a meteor crater in Arizona, and the mineral was named stishovite (3). Stishovite was once the hardest known oxide material (4), and its hardness measured by indentation, 32 to 33 GPa, still rivals those of the hardest materials (5, 6). Unfortunately, its brittleness (that is, low toughness) has thus far hindered practical applications.

Recently, Nishiyama *et al.* synthesized a nanostructural form of stishovite named nano-polycrystalline stishovite (NPS), which exhibits remarkably high fracture toughness of about 10 MPa·m^1/2, according to Vickers indentation fracture measurements, while retaining high hardness (7, 8). Because NPS is made by simply applying high pressure to Earth-abundant silica glass, it could provide a sustainable supply of high-performance ceramics in the future. Subsequent micromechanical tests using microcantilever beam specimens showed that the underlying toughening mechanism is effective even when a crack length is on the order of nanometers (9). Electron microscopy and x-ray absorption near-edge structure spectroscopy identified the existence of amorphous silica within subnanometers from fracture surfaces (8). Furthermore, the amount of amorphous silica near the fracture surfaces was shown to correlate positively with the fracture toughness (8). This led to our proposal of an amorphization-induced toughening mechanism (8, 9). Namely, under high tensile stress in front of a crack tip, metastable stishovite undergoes structural transformation to amorphous silica that is more stable under ambient conditions. The stishovite-to-amorphous transformation is accompanied by a volume expansion of ~100%, and the swollen transformation zone screens and self-heals the crack (8, 9). Although plausible, for this transformation-toughening mechanism

(10) to operate, the amorphization of stishovite must proceed rapidly to catch up with the crack tip that is moving fast at a speed above nanometers per picosecond (or 10³ m/s). However, no theoretical or experimental evidence exists for this rapid amorphization of stishovite under tension.

For millennia, amorphization has been commonly realized by rapid cooling of liquid, that is, by thermal means. The seminal discovery of amorphization of ice under compression by Mishima *et al.* (11) spurred active research on alternative mechanical pathways to amorphization. For SiO₂, pressure-induced amorphization of α-quartz and coesite crystals was reported by Hemley *et al.* (12), which was later studied using atomistic simulations (13) along with other high-pressure transformations (14). The possibility of a similar amorphization process by decompressing high-pressure synthesized solids was suggested by Jeanloz (15), and its thermodynamics has been discussed extensively over the last 30 years (16). That is, upon rapid decompression, a crystal that was synthesized under high pressure can cross a metastable fusion curve to undergo amorphization (16). Despite this thermodynamic understanding, little is known about the nonequilibrium dynamics by which the atoms rearrange during tensile amorphization.

RESULTS

To elucidate tensile amorphization dynamics of stishovite, we perform quantum molecular dynamics (QMD) simulations, which follow the trajectories of all atoms while computing interatomic forces quantum mechanically from first principles (see Materials and Methods). In QMD simulations, the equations of motion are numerically integrated in a canonical ensemble at a temperature of 300 K. Atomistic behaviors under tension are investigated by isotropic expansion of a simulation cell that contains single-crystalline stishovite (Fig. 1A). First, the stishovite with an equilibrium mass density of $\rho = 4.1$ g/cm³ (which is close to the experimental density of 4.3 g/cm³) is thermalized for 1 ps. Subsequently, the side lengths of the simulation cell are stretched by 1% for every 1 ps, which corresponds to a strain rate of $d\varepsilon/dt = 10^{10}$ s⁻¹ to mimic rapidly rising tension in front of a crack tip. Figure 1B shows time evolution of the pressure for 11 ps. For expansion up to 7 ps, we observe a nearly elastic response with more negative pressure for lower mass density. The pressure reaches −30 GPa at 7 ps. Upon further expansion, we observe a sudden increase in pressure from large negative to positive

[1]Collaboratory for Advanced Computing and Simulations, Department of Physics and Astronomy, Department of Computer Science, Department of Chemical Engineering and Materials Science, and Department of Biological Sciences, University of Southern California, Los Angeles, CA 90089–0242, USA. [2]Department of Physics, Kumamoto University, Kumamoto 860-8555, Japan. [3]Materials and Structures Laboratory, Tokyo Institute of Technology, 4259 Nagatsuta, Midori, Yokohama 226-8503, Japan. [4]Deutsches Elektronen-Synchrotron (DESY), Hamburg 22607, Germany.
*Corresponding author. Email: anakano@usc.edu
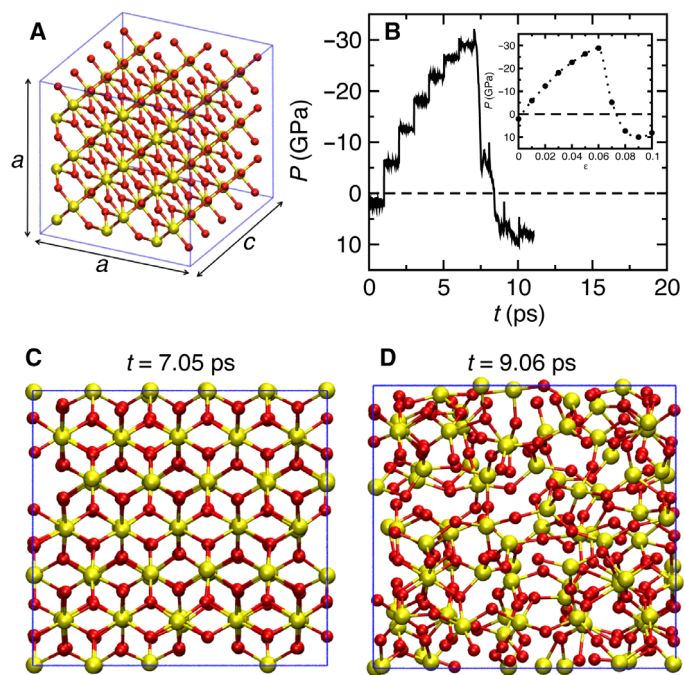
Fig. 1. Rapid amorphization of stishovite under tension. (**A**) Simulation cell at $\rho = 4.1$ g/cm^3. The yellow and red spheres are Si and O atoms, respectively. (**B**) Time evolution of the pressure. Inset: Final pressure for each strain value. (**C** and **D**) Snapshots of single-crystalline stishovite at $t = 7.05$ ps (C) and amorphized SiO$_2$ at $t = 9.06$ ps (D).

values. This transition is accompanied by disordering of atomic arrangements. Figure 1 (C and D) shows snapshots of atomic configurations before and after the structural transformation, respectively. Here, an important quantity is the time scale τ associated with the structural transformation. Figure 1B shows that the negative-to-positive pressure response completes within $\tau \sim 2$ ps. Movie S1 shows the rapid disordering process. In summary, at a critical tensile pressure of -30 GPa, stishovite crystal undergoes rapid disordering within 2 ps to release tension. With a typical speed on the order of $v = 5 \times 10^3$ m/s, a crack propagates by a distance of $h = v\tau = 10$ nm within this time frame. This distance is consistent with the experimentally measured thickness of transformation zones, and thus, the disordering dynamics found here are sufficiently fast to account for experimentally observed transformation toughening (8, 9). The critical tension of -30 GPa in stishovite is similar to that (-18 GPa) for tensile amorphization of CaSiO$_3$ and MgSiO$_3$ perovskites (17). The calculated critical tension is also consistent with a simple thermodynamic estimate based on measured activation energy and dilation strain associated with the amorphization of stishovite (18).

To study the energetics of the structural transformation, Fig. 2A shows the energy (E)–density (ρ) relationship. The solid black circles correspond to the E-ρ relation of stishovite crystal, which was sampled by QMD simulation before the structural transformation (shown in Fig. 1) occurs. The third-order Birch-Murnaghan (BM) equation of state (EoS) fitting gives a bulk modulus of $B = 280$ GPa and its pressure derivative $B' = 4.9$, which are in reasonable agreement with experimental values for stishovite ($B = 299$ to 313 GPa and $B' = 3.8$ to 4.4) (19). Figure 2B shows the calculated virial pressure (P) as a function of ρ. The slope of the P-ρ curve for stishovite in Fig. 2B (solid black circles) is consistent with the corresponding curvature of the E-ρ curve in Fig. 2A. In contrast to the robust energetics of the stishovite phase, that of the transformed phase is highly sensitive to subtle simulation conditions, such as tem-

perature control. For example, transitions to slightly different structures and energies are obtained from simulations without and with temperature control. The open blue squares in Fig. 2A show the E-ρ relation for the transformed phase obtained by QMD simulations. The solid blue squares in Fig. 2A are obtained instead by QMD without temperature control. This scattered E-ρ plot (that is, open blue squares versus solid blue squares in Fig. 2A) indicates a rough energy landscape that is composed of many shallow metastable basins (20) for the tensile-origin amorphous phase. The potential energy of the final configuration obtained without temperature control (for example, data point labeled f in Fig. 2A) is lower than that obtained with temperature control (for example, data point labeled d in Fig. 2A) for the same mass density. Because the temperature becomes higher without the thermostat, energy barriers are overcome to transform into more stable structures. Furthermore, when we expand the simulation cell volume starting from a configuration obtained with temperature control (labeled d in Fig. 2A), the energy of the final configuration drops considerably (labeled e in Fig. 2A), indicating an escape from a metastable energy basin to a more stable one. To obtain the E-ρ relation of these more stable structures, we next perform a series of QMD simulations starting from one of the lower-energy configurations (labeled f in Fig. 2A), where the configuration is relaxed while changing the simulation cell volume gradually. In Fig. 2A, the solid red triangles show the E-ρ relationship for the stable branch of disordered structures. The BM-EoS fitting for the corresponding amorphous phase gives $B = 40.7$ GPa and the minimum energy density $\rho_0 = 2.4$ g/cm^3. The corresponding P-ρ relation for the amorphous phase is shown by solid red triangles in Fig. 2B.

Because of the short time scale of QMD simulations, the above simulation procedure likely does not probe the eventual low-density phase that may be reached in longer time. To explore this issue, we perform another set of QMD simulations, in which normal amorphous silica is prepared using a conventional melt-quench procedure, that is, by thermal means. Solid green triangles in Fig. 2A show the resulting E-ρ relation. The BM-EoS fitting for the corresponding amorphous phase gives $B = 29.1$ GPa, and the minimum energy density $\rho_0 = 2.1$ g/cm^3 is close to that of ordinary silica glass. The calculated energy of the normal glass is 0.33 eV/SiO$_2$ lower than that of the stishovite phase, which is in good agreement with the experimentally known energetics (16). These simulation results suggest a two-step amorphization mechanism via an intermediate state akin to "high-density" silica glass (21–24) before the final transformation to normal glass. Since the pioneering work by Bridgman and Šimon (21), permanent densification of silica glass using high pressure has been well studied experimentally (22, 24). Vastly different structural, mechanical, and vibrational properties of the high-density silica glass from those of normal, low-density silica glass have led to the suggestion of "amorphous polymorphism" (22). Here, this amorphous polymorphism has been probed dynamically as an intermediate state during tensile amorphization. A similar transition between high- and low-density forms of amorphous material also has been observed in silicon (25).

To characterize the stishovite structure (corresponding to the solid black circles in Fig. 2A) and the intermediate high-density amorphous structure (corresponding to the open blue squares in Fig. 2A) in the QMD simulations, Fig. 2 (C to F) shows the Si-O partial pair distribution function (26), $g_{SiO}(r)$, at various densities. We see a shift of the first peak position from 1.8 to 1.6 Å as the density is lowered. In addition, the second and higher peaks are smeared out below 3.2 g/cm^3. These structural features are consistent with those of amorphous silica (26). Figure S1 shows $g_{SiSi}(r)$ and $g_{OO}(r)$ at various densities. We also calculate the
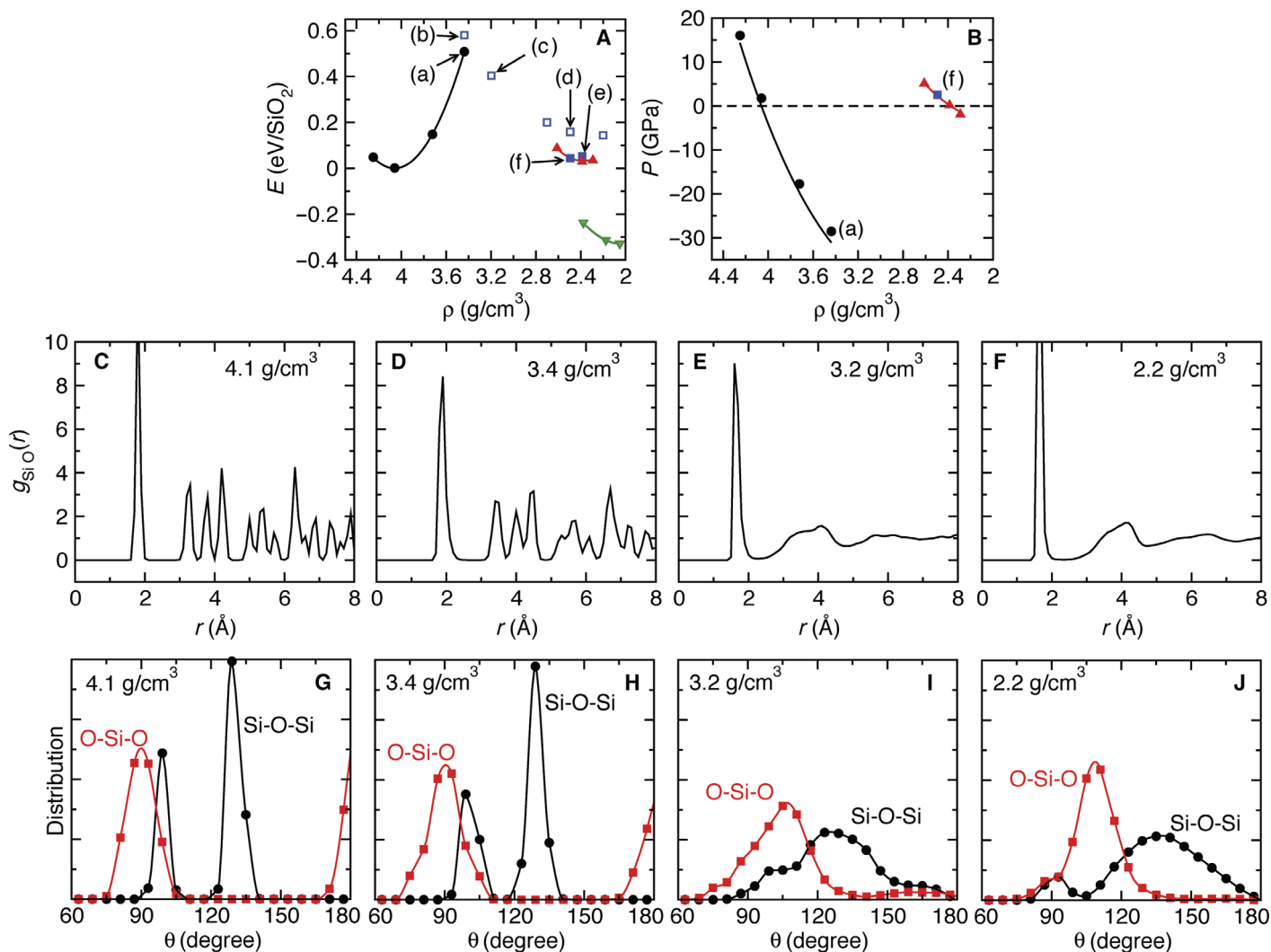
Fig. 2. Stishovite-to-amorphous transformation. (**A**) Energy-density relation obtained by QMD simulations. The energy is relative to the minimum energy of single-crystalline stishovite. The solid black circles denote the stishovite crystalline phase, whereas the open blue squares are the amorphous phase. The amorphous-phase data points denoted by open and solid squares are obtained by QMD simulations with and without temperature control, respectively. The results labeled (b) and (e) are obtained by simulations that start from the atomic configurations of (c) and (d) by changing the mass density to $\rho = 3.4$ and 2.4 g/cm^3, respectively. The solid red triangles are obtained by gradually changing the volume from that of the atomic configuration (f). The solid green triangles denote normal amorphous silica prepared by a melt-quench procedure. The black, red, and green curves show fitting using a third-order BM-EoS. (**B**) Pressure-density relation obtained by QMD simulations for the stishovite (solid black circles) and amorphous (solid blue squares and solid red triangles) phases. The black and red curves are the derivative of the BM-EoS curves in (A) with respect to volume, respectively, for the stishovite and amorphous phases. (**C** to **F**) Mass-density dependence of partial pair distribution function $g_{SiO}(r)$. (**G** to **J**) Mass-density dependence of bond-angle distributions $\theta_{Si-O-Si}$ and θ_{O-Si-O}.

distribution of bond angles $\theta_{Si-O-Si}$ and θ_{O-Si-O} at various densities. Overall, broadening of peaks is observed at lower densities, signifying progressive disordering of atomic positions. The calculated θ_{O-Si-O} in Fig. 2 (G to J) exhibits two peaks at 90° and 180° at high densities and a single peak at 109° at low densities. The former is consistent with the stishovite structure composed of an octahedral SiO$_6$ unit, whereas the latter is consistent with the amorphous silica structure composed of a tetrahedral SiO$_4$ unit (26). In Fig. 2 (G to J), the change of $\theta_{Si-O-Si}$ from a double-peak distribution at 100° and 130° at high densities and a single-peak distribution at 137° is also consistent with $\theta_{Si-O-Si}$ in known stishovite and amorphous silica structures (26).

To further characterize the intermediate amorphous structure (corresponding to the open blue squares in Fig. 2A), Fig. 3 (A to C) shows the fraction of Si atoms that are connected to four, five, and six

neighbor O atoms at various mass densities. The results show that 6% of Si atoms remain fivefold-coordinated at 2.2 g/cm^3 (this is in contrast to normal glass, where nearly all Si atoms are fourfold-coordinated). The local structures around Si atoms can be classified into mainly three types of SiO$_x$ ($x = 4$, 5, and 6) units (Fig. 3, D to F). In stishovite crystal, all Si atoms are connected to six O atoms to form octahedral SiO$_6$ units (Fig. 3F). However, an amorphous SiO$_2$ structure is composed mostly of tetrahedral SiO$_4$ units (Fig. 3D) (26). In addition, pyramidal SiO$_5$ units are found in the intermediate glass in our simulation (Fig. 3E). It is conceivable that the O-Si-O bond-angle distributions around 90° are caused by residuals of SiO$_6$ and SiO$_5$ units. In normal SiO$_2$ glass, fourfold-coordinated Si and twofold-coordinated O atoms form a network structure of corner-sharing SiO$_4$ tetrahedral units. However, some anomalous local structures are found in the intermediate amorphous
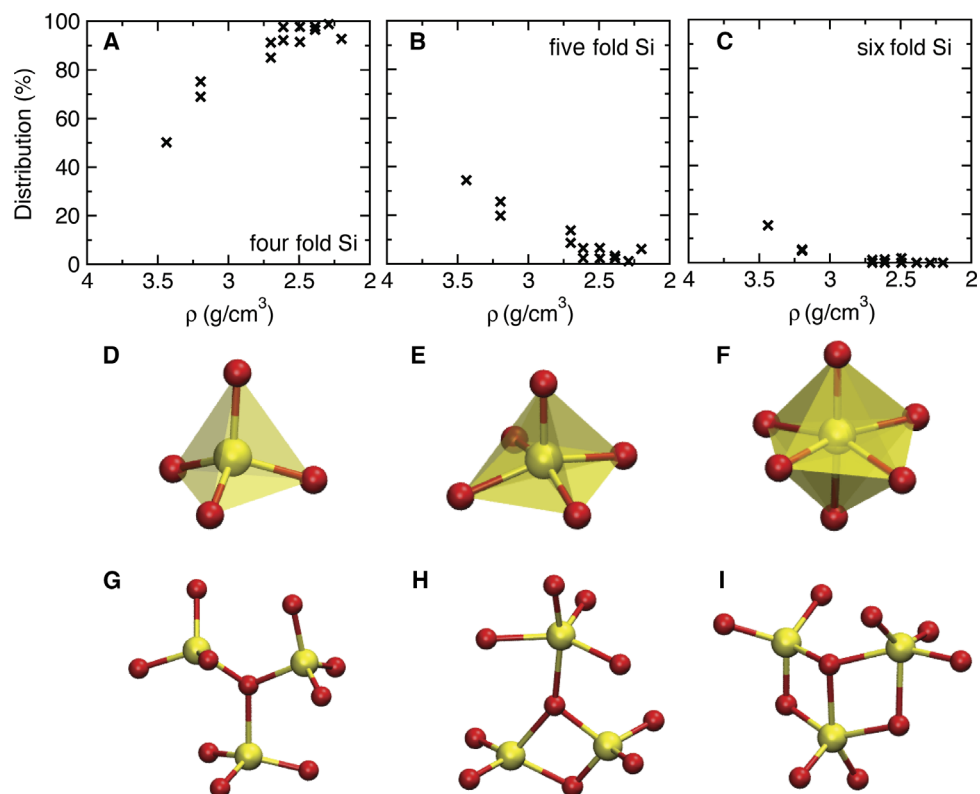
Fig. 3. Tension-derived high-density amorphous silica. (A to C) Average coordination number distributions as a function of density for Si atoms with cutoff distance $r_{Si-O} = 2.2$ Å. (D to F) Snapshots of a SiO_4 tetrahedral unit (D), SiO_5 pyramidal unit (E), and SiO_6 octahedral unit (F). The yellow and red spheres are Si and O atoms, respectively, whereas the polygonal surfaces are represented by yellow planes. (G to I) Snapshots of local structures found in the intermediate amorphous structure formed by three SiO_x units sharing O atoms: three corner-sharing tetrahedra (G), a pair of edge-shared tetrahedra (each sharing a corner with a pyramid) (H), and a corner-sharing tetrahedron-pyramid pair (each sharing an edge with another pyramid) (I).

phase. Among these structures, a threefold-coordinated O atom shared by three SiO_x units (Fig. 3G) and an edge-sharing structure consisting of two SiO_x units (Fig. 3H) have been reported (27, 28). In addition, we find a pair of two edge-shared structures composed of three SiO_x units (Fig. 3I). This structure is unique to the intermediate amorphous phase, which inherits SiO_5 and SiO_6 units from stishovite. Edge-shared tetrahedra are known to cause high strain and hence high energy. Accordingly, they are not observed in normal glass. Here, these edge-shared polyhedral units are observed only transiently in intermediate metastable amorphous structures, likely because of insufficient relaxation.

Next, we study the reaction pathways and associated activation energies of the stishovite-to-amorphous transformation. The energy profile along the reaction coordinate is calculated at various densities using the nudged elastic band (NEB) method. The initial and final states for these calculations are the stishovite and amorphous structures taken from QMD simulations at densities of 3.4 and 3.2 g/cm³, respectively. At each density, scaled coordinates of these configurations are used as a starting point of structural relaxation. The fully relaxed minimum energy stishovite and amorphous structures are then used as the initial state (corresponding to reaction coordinate $\lambda = 0$) and final state ($\lambda = 1$) of NEB calculation, respectively. Here, λ is the image index ($i = 0, 1, …, N_{image}$) divided by the number of images but 1, N_{image}, used in the NEB calculation. Figure 4A shows the energy profile for various densities. For $\rho = 4.1$ g/cm³ (that is, stishovite density) and 3.7 g/cm³, the stishovite-to-amorphous transformation is endothermic, with a reaction energy of

1.1 and 0.72 eV/SiO_2, respectively. At $\rho = 3.4$ g/cm³, the reaction energy becomes nearly zero, with an activation energy of 0.2 eV/SiO_2, signifying a first-order phase transition. Below this density, the stishovite phase becomes dynamically unstable, and the exothermic amorphization becomes barrier-less, as shown for the case of $\rho = 3.2$ g/cm³ in Fig. 4A.

Note that the structural transformations in Fig. 4A transform stishovite into intermediate amorphous structures. Subsequent structural relaxation brings these structures to lower-energy amorphous structures. To study the latter structural transformation, we take structures (d) and (e) in Fig. 2A as the initial and final states to perform another NEB calculation. The result in Fig. 4B shows that this amorphous-to-amorphous transformation is weakly exothermic, with a very low activation energy of 0.047 eV/SiO_2. This low activation energy is thermally overcome readily at room temperature, and it may be difficult to observe the intermediate amorphous structure in postfracture specimens.

To understand the amorphization pathway, Fig. 4 (E to H) shows snapshots of atomic configurations at reaction coordinate $\lambda = 0, 0.33, 0.67$, and 1 along the stishovite-to-amorphous transformation at $\rho = 3.4$ g/cm³. Movie S2 shows the change of atomic configurations from the stishovite to amorphous phases. From $\lambda = 0$ to 0.33, we observe breakage of an Si-O bond (pointed by the green arrow in Fig. 4E). This is followed by breakage of a second Si-O bond (pointed by the green arrow in Fig. 4F) from $\lambda = 0.33$ to 0.67. These bond-breaking events are reflected in the change of the Si coordination number. Figure 4C shows that the distribution of Si coordination number changes rapidly from $\lambda = 0$ to 0.67, after which it remains nearly constant. The
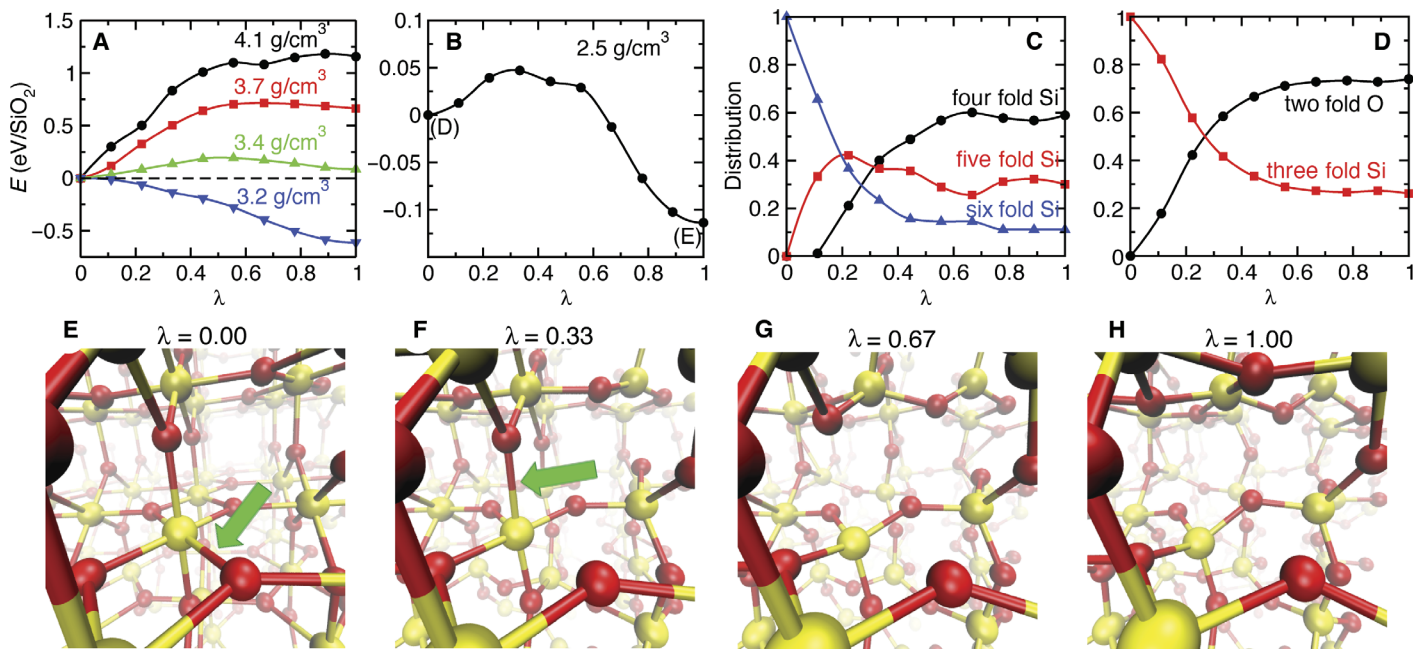
Fig. 4. Amorphization pathways. (**A**) Energy profile from stishovite crystal (reaction coordinate $\lambda = 0$) to high-density amorphous phase ($\lambda = 1$) obtained by NEB calculation. The energy for configuration 0 is set to zero. (**B**) Energy profile for a subsequent amorphous-to-amorphous transformation corresponding to configurations (d) to (e) in Fig. 2A. (**C** and **D**) Distributions of the coordination number of Si (C) and O (D) atoms along the reaction pathway, which are calculated using a cutoff distance $r_{Si-O} = 2.2$ Å. (**E** to **H**) Snapshots of atomic configurations at $\lambda = 0$ (E), 0.33 (F), 0.67 (G), and 1 (H) along the stishovite-to-amorphous transformation at $\rho = 3.4$ g/cm^3, corresponding to a transition from (a) to (b) that is shown in Fig. 2A.

distribution of the O coordination number exhibits a similar rapid change below $\lambda = 0.67$ (Fig. 4D). Figure S2 (A to D) shows the change of Si and O coordination number distributions for $\lambda = 0$, 0.33, 0.67, and 1, respectively. During these successive bond-breaking events, we observe little structural relaxation. After completing the bond-breaking events, we then observe massive structural relaxation, which is apparent by comparing Fig. 4 (G and H) for $\lambda = 0.67$ to 1, respectively. This structural relaxation results in the change of bond-angle distribution in fig. S2 (E to H), which assumes a typical amorphous shape consisting of a single broad peak, which, in turn, indicates massive rotational motions. Namely, we have found a two-step amorphization mechanism of stishovite, that is, Si-O bond breakage followed by bond rotations. This mechanism can be thought of as a reverse process of that hypothesized for the pressure-induced crystal-to-crystal structural transformation between cristobalite and stishovite, which consists of tetrahedral rotations, followed by atom shifts (29, 30). However, because of energetically degenerate pathways, the structural transformation gives rise to an amorphous structure instead of the crystal-to-crystal transformation studied before.

Note that these bond-breaking and bond-rotation events only involve small atomic displacements. Figure S3 shows the average mean square displacement (MSD) of Si and O atoms along the reaction coordinate during NEB calculation of stishovite-to-amorphous transformation at $\rho = 3.4$ g/cm^3. During the entire amorphization process, both Si and O atoms undergo very small displacement under 1 Å. The magnitude of this displacement is nearly identical with that observed in MD simulations of crystalline-to-amorphous transition in silicate perovskite (17). This result indicates that the tensile amorphization of stishovite is a displacive transformation that only involves short-distance collective motions of atoms rather than diffusive long-distance movements. As a

result, the amorphization occurs in a very short time (<2 ps) to facilitate efficient transformation toughening and self-heal fast-moving cracks.

Thermodynamically, tensile amorphization of stishovite is well understood in terms of the very high Gibbs free energy of stishovite compared with that of amorphous silica (as demonstrated in Fig. 2A) (16). What is new here is the extremely small time scale associated with this structural transformation. Because of short-distance collective motions of atoms in the displacive amorphization pathway found in our simulations, the tensile amorphization of stishovite occurs extremely fast on the time scale of picoseconds. Because of recent experimental progress in ultrafast diffraction using x-ray free-electron laser (31), the proposed amorphization pathway may become amenable for experimental validation in the future. Note that, in contrast to tensile amorphization of the high-pressure stishovite phase reported here, similar decompression leads to pore formation and fracture instead in low-density silica (32, 33).

DISCUSSION
Although the rapid tensile amorphization found in our QMD simulations accounts for the experimentally observed toughening in NPS at the nanometer scale (7, 8), this mechanism by itself cannot explain why the crack growth resistance continues to increase as a function of crack extension at the micrometer scale (9). To understand this so-called R-curve, we need to incorporate the effects of microstructures, such as grain boundaries and dislocations, where heterogeneous nucleation of the amorphous phase likely takes place. Studying these effects would require multimillion-atom MD simulations, which are only possible using more empirical interatomic potentials. For example, large MD simulations revealed a crossover of indentation response in nanocrystalline SiC from intergranular continuous deformation to intragrain discrete

deformation at a critical length that is a fraction of the grain size (*34*). The crossover arises from the interplay between cooperative grain sliding, grain rotations, and stick-slip–like intergranular dislocation formation. These unique mechanical properties of nanocrystalline materials are essentially controlled by interphases (*35*) [or complexions (*36*, *37*)] within a few nanometers from grain boundaries that have distinct structures from bulk phases (*34*, *38*, *39*). Enabled by the fast amorphization-toughening mechanism found in this work, the synergy between hardness and toughness may be operating widely in other nano-polycrystalline materials made of high pressure–synthesized hard solids. A potential candidate is post-stishovite silica (*5*), for which recent experiments have shown peculiar phase transition kinetics (*40*).

MATERIALS AND METHODS
QMD simulation method
The electronic states were calculated using the projector augmented-wave (PAW) method within a framework of density functional theory (*41*, *42*). Projector functions were generated for the $3s$ and $3p$ states of Si and for the $2s$ and $2p$ states of O. The generalized gradient approximation (GGA) was used for the exchange-correlation energy (*43*). Although hybrid exact-exchange functionals improve some physical quantities, such as band gaps and excitonic interactions, we found that GGA reliably produced interatomic forces, which is the focus of this paper (*44*). The momentum-space formalism was used (*45*), where the plane wave cutoff energies were 30 and 300 Ry for the electronic pseudowave functions and pseudocharge density, respectively. A supercell, including 270 atoms (90 Si + 180 O), which corresponded to $3 \times 3 \times 5$ crystalline unit cells, was used as the initial configuration of single-crystalline stishovite. The periodic boundary conditions were applied in all directions. The Γ point was used for Brillouin zone sampling for electronic structure calculations. With this method, the equilibrium mass density was $\rho = 4.1$ g/cm^3, with side lengths of $L_x = L_y = 12.74$ Å and $L_z = 13.63$ Å. In QMD simulations, the equations of motion were numerically integrated with a time step of 1.936 fs in a canonical ensemble. The temperature was kept to 300 K using the Nosé-Hoover thermostat technique (*46*, *47*). Energy barriers from the stishovite to amorphous phases were calculated using the NEB method (*48*). Low-density amorphous silica was prepared by a melt-quench procedure in an isothermal-isobaric ensemble with the pressure $P = 0$ GPa, starting from cristobalite crystal. First, the silica was heated to 4000 K for 2.9 ps and then quenched to 2000 K with a cooling rate of 86 K/ps. Because there were almost no defects at 2000 K, the temperature was then set to 300 K and thermalized for 8.7 ps. The amorphous silica thus obtained had the equilibrium mass density of 2.1 g/cm^3 under ambient conditions. The data points shown as green triangles in Fig. 2A were obtained by compression of this configuration. Note that although other simulation methods, such as stochastic quenching, were effective in widely exploring energy landscapes, the purpose of this paper was to quantify the real dynamics and time scale of structural transformations, for which QMD was most suitable (*49*, *50*).

Bond-overlap population analysis
To quantify the change in the bonding properties of atoms, we used bond-overlap population analysis (*51*) by expanding the electronic wave functions in an atomic orbital basis set (*52*). On the basis of the formulation generalized to the PAW method (*53*), we obtained the gross population $Z_i(t)$ for the ith atom and the bond-overlap population $O_{ij}(t)$ for a pair of ith and jth atoms as a function of time t. From $Z_i(t)$, we esti-

mated the charge of atoms, and $O_{ij}(t)$ gave a semiquantitative estimate of the strength of covalent bonding between atoms. As the atomic basis orbitals, we used numerical pseudoatomic orbitals, which were obtained for a chosen atomic energy so that the first node occurred at the desired cutoff radius (*54*). To increase the efficiency of the expansion, the numerical basis orbitals were augmented with the split-valence method (*55*). The resulting charge spillage, which estimated the error in the expansion, was only 0.15%, indicating the high quality of the basis orbitals.

SUPPLEMENTARY MATERIALS
Supplementary material for this article is available at http://advances.sciencemag.org/cgi/content/full/3/5/e1602339/DC1

movie S1. Rapid amorphization of stishovite upon volume expansion at a critical tension of −30 GPa.
movie S2. Change of atomic configurations along the reaction pathway from the stishovite to amorphous phases at ρ = 3.4 g/cm^3.
fig. S1. Si-Si and O-O pair distributions at various densities.
fig. S2. Change of coordination numbers and bond-angle distributions during the stishovite-to-amorphous transformation.
fig. S3. Atomic displacements during the stishovite-to-amorphous transformation.

REFERENCES AND NOTES
1. K. H. Wedepohl, The composition of the continental-crust. *Geochim. Cosmochim. Acta* **59**, 1217–1232 (1995).
2. S. M. Stishov, S. V. Popova, New dense polymorphic modification of silica. *Geokhimiya* **10**, 839–937 (1961).
3. E. C. T. Chao, J. J. Fahey, J. Littler, D. J. Milton, Stishovite, SiO₂, a very high pressure new mineral from meteor crater, Arizona. *J. Geophys. Res.* **67**, 419–421 (1962).
4. J. M. Leger, J. Haines, M. Schmidt, J. P. Petitet, A. S. Pereira, J. A. H. da Jornada, Discovery of hardest known oxide. *Nature* **383**, 401 (1996).
5. L. S. Dubrovinsky, N. A. Dubrovinskaia, V. Swamy, J. Muscat, N. M. Harrison, R. Ahuja, B. Holm, B. Johansson, The hardest known oxide. *Nature* **410**, 653–654 (2001).
6. V. V. Brazhkin, M. Grimsditch, I. Guedes, N. A. Bendeliani, T. I. Dyuzheva, L. M. Lityagina, Elastic moduli and the mechanical properties of stishovite single crystals. *Phys. Usp.* **45**, 447–448 (2002).
7. N. Nishiyama, S. Seike, T. Hamaguchi, T. Irifune, M. Matsushita, M. Takahashi, H. Ohfuji, Y. Kono, Synthesis of nanocrystalline bulk SiO₂ stishovite with very high toughness. *Scr. Mater.* **67**, 955–958 (2012).
8. N. Nishiyama, F. Wakai, H. Ohfuji, Y. Tamenori, H. Murata, T. Taniguchi, M. Matsushita, M. Takahashi, E. Kulik, K. Yoshida, K. Wada, J. Bednarcik, T. Irifune, Fracture-induced amorphization of polycrystalline SiO₂ stishovite: A potential platform for toughening in ceramics. *Sci. Rep.* **4**, 6558 (2014).
9. K. Yoshida, F. Wakai, N. Nishiyama, R. Sekine, Y. Shinoda, T. Akatsu, T. Nagoshi, M. Sone, Large increase in fracture resistance of stishovite with crack extension less than one micrometer. *Sci. Rep.* **5**, 10993 (2015).
10. R. M. Mcmeeking, A. G. Evans, Mechanics of transformation-toughening in brittle materials. *J. Am. Ceram. Soc.* **65**, 242–246 (1982).
11. O. Mishima, L. D. Calvert, E. Whalley, 'Melting ice' I at 77 K and 10 kbar: A new method of making amorphous solids. *Nature* **310**, 393–395 (1984).
12. R. J. Hemley, A. P. Jephcoat, H. K. Mao, L. C. Ming, M. H. Manghnani, Pressure-induced amorphization of crystalline silica. *Nature* **334**, 52–54 (1988).
13. R. M. Wentzcovitch, C. da Silva, J. R. Chelikowsky, N. Binggeli, A new phase and pressure induced amorphization in silica. *Phys. Rev. Lett.* **80**, 2149–2152 (1998).
14. S. Tsuneyuki, Y. Matsui, H. Aoki, M. Tsukada, New pressure-induced structural transformations in silica obtained by computer-simulation. *Nature* **339**, 209–211 (1989).
15. R. Jeanloz, European high-pressure research conference. *Eos* **65**, 1245–1246 (1984).
16. P. Richet, Superheating, melting and vitrification through decompression of high-pressure minerals. *Nature* **331**, 56–58 (1988).
17. M. Hemmati, A. Chizmeshya, G. H. Wolf, P. H. Poole, J. Shao, C. A. Angell, Crystalline-amorphous transition in silicate perovskites. *Phys. Rev. B* **51**, 14841–14848 (1995).
18. K. Yoshida, N. Nishiyama, M. Sone, F. Wakai, Strength and toughness of nanocrystalline SiO₂ stishovite toughened by fracture-induced amorphization. *Acta Mater.* **124**, 316–324 (2017).
19. F. Jiang, G. D. Gwanmesia, T. I. Dyuzheva, T. S. Duffy, Elasticity of stishovite and acoustic mode softening under high pressure by Brillouin scattering. *Phys. Earth Planet. In.* **172**, 235–240 (2009).

20. A. Kushima, X. Lin, J. Li, X. Qian, J. Eapen, J. C. Mauro, P. Diep, S. Yip, Computing the viscosity of supercooled liquids. II. Silica and strong-fragile crossover behavior. *J. Chem. Phys.* **131**, 164505 (2009).

21. P. W. Bridgman, I. Šimon, Effects of very high pressures on glass. *J. Appl. Phys.* **24**, 405–413 (1953).

22. M. Grimsditch, Polymorphism in amorphous SiO_2. *Phys. Rev. Lett.* **52**, 2379–2381 (1984).

23. W. Jin, R. K. Kalia, P. Vashishta, J. P. Rino, Structural transformation, intermediate-range order, and dynamical behavior of SiO_2 glass at high-pressures. *Phys. Rev. Lett.* **71**, 3146–3149 (1993).

24. Y. Inamura, Y. Katayama, W. Utsumi, K. Funakoshi, Transformations in the intermediate-range structure of SiO_2 glass under high pressure and temperature. *Phys. Rev. Lett.* **93**, 015501 (2004).

25. S. K. Deb, M. Wilding, M. Somayazulu, P. F. McMillan, Pressure-induced amorphization and an amorphous–amorphous transition in densified porous silicon. *Nature* **414**, 528–530 (2001).

26. P. Vashishta, R. K. Kalia, J. P. Rino, I. Ebbsjö, Interaction potential for SiO_2: A molecular-dynamics study of structural correlations. *Phys. Rev. B* **41**, 12197–12209 (1990).

27. B. C. Bunker, D. M. Haaland, T. A. Michalske, W. L. Smith, Kinetics of dissociative chemisorption on strained edge-shared surface-defects on dehydroxylated silica. *Surf. Sci.* **222**, 95–118 (1989).

28. V. O. Sokolov, V. B. Sulimov, Threefold coordinated oxygen atom in silica glass. *J. Non-Cryst. Solids* **217**, 167–172 (1997).

29. B. Silvi, L.-H. Jolly, P. D'Arco, Pseudopotential periodic Hartree-Fock study of the cristobalite to stishovite phase transition. *J. Mol. Struct. Theochem* **92**, 1–9 (1992).

30. M. O'Keeffe, B. G. Hyde, Cristobalites and topologically-related structures. *Acta Cryst.* **32**, 2923–2936 (1976).

31. A. E. Gleason, C. A. Bolme, H. J. Lee, B. Nagler, E. Galtier, D. Milathianaki, J. Hawreliak, R. G. Kraus, J. H. Eggert, D. E. Fratanduono, G. W. Collins, R. Sandberg, W. Yang, W. L. Mao, Ultrafast visualization of crystallization and grain growth in shock-compressed SiO_2. *Nat. Commun.* **6**, 8191 (2015).

32. A. Nakano, R. K. Kalia, P. Vashishta, Growth of pore interfaces and roughness of fracture surfaces in porous silica: Million particle molecular-dynamics simulations. *Phys. Rev. Lett.* **73**, 2336–2339 (1994).

33. Y. Chen, Z. Lu, K.-i. Nomura, W. Wang, R. K. Kalia, A. Nakano, P. Vashishta, Interaction of voids and nanoductility in silica glass. *Phys. Rev. Lett.* **99**, 155506 (2007).

34. I. Szlufarska, A. Nakano, P. Vashishta, A crossover in the mechanical response of nanocrystalline ceramics. *Science* **309**, 911–914 (2005).

35. D. R. Clarke, On the equilibrium thickness of intergranular glass phases in ceramic materials. *J. Am. Ceram. Soc.* **70**, 15–22 (1987).

36. S. J. Dillon, M. Tang, W. C. Carter, M. P. Harmer, Complexion: A new concept for kinetic engineering in materials science. *Acta Mater.* **55**, 6208–6218 (2007).

37. M. Baram, D. Chatain, W. D. Kaplan, Nanometer-thick equilibrium films: The interface between thermodynamics and atomistics. *Science* **332**, 206–209 (2011).

38. H.-P. Chen, R. K. Kalia, E. Kaxiras, G. Lu, A. Nakano, K.-i. Nomura, A. C. T. van Duin, P. Vashishta, Z. Yuan, Embrittlement of metal by solute segregation-induced amorphization. *Phys. Rev. Lett.* **104**, 155502 (2010).

39. K. Shimamura, F. Shimojo, R. K. Kalia, A. Nakano, P. Vashishta, Bonding and structure of ceramic-ceramic interfaces. *Phys. Rev. Lett.* **111**, 066103 (2013).

40. T. Kubo, T. Kato, Y. Higo, K.-i. Funakoshi, Curious kinetic behavior in silica polymorphs solves seifertite puzzle in shocked meteorite. *Sci. Adv.* **1**, e1500075 (2015).

41. G. Kresse, D. Joubert, From ultrasoft pseudopotentials to the projector augmented-wave method. *Phys. Rev. B* **59**, 1758–1775 (1999).

42. P. E. Blöchl, Projector augmented-wave method. *Phys. Rev. B* **50**, 17953–17979 (1994).

43. J. P. Perdew, K. Burke, M. Ernzerhof, Generalized gradient approximation made simple. *Phys. Rev. Lett.* **77**, 3865–3868 (1996).

44. F. Shimojo, S. Hattori, R. K. Kalia, M. Kunaseth, A. Nakano, K.-i. Nomura, S. Ohmura, K. Shimamura, P. Vashishta, A divide-conquer-recombine algorithmic paradigm for large spatiotemporal quantum molecular dynamics simulations. *J. Chem. Phys.* **140**, 18A529 (2014).

45. J. Ihm, A. Zunger, M. L. Cohen, Momentum-space formalism for the total energy of solids. *J. Phys. C* **12**, 4409–4422 (1979).

46. S. Nosé, A unified formulation of the constant temperature molecular dynamics methods. *J. Chem. Phys.* **81**, 511–519 (1984).

47. W. G. Hoover, Canonical dynamics: Equilibrium phase-space distributions. *Phys. Rev. A* **31**, 1695–1697 (1985).

48. G. Henkelman, H. Jónsson, Improved tangent estimate in the nudged elastic band method for finding minimum energy paths and saddle points. *J. Chem. Phys.* **113**, 9978–9985 (2000).

49. E. Holmström, N. Bock, T. Peery, E. Chisolm, R. Lizárraga, G. De Lorenzi-Venneri, D. Wallace, Structure discovery for metallic glasses using stochastic quenching. *Phys. Rev. B* **82**, 024203 (2010).

50. X. Jiang, C. Århammar, P. Liu, J. J. Zhao, R. Ahuja, The R3-carbon allotrope: A pathway towards glassy carbon under high pressure. *Sci. Rep.* **3**, 1877 (2013).

51. R. S. Mulliken, Electronic population analysis on LCAO–MO molecular wave functions. I. *J. Chem. Phys.* **23**, 1833–1840 (1955).

52. M. D. Segall, R. Shah, C. J. Pickard, M. C. Payne, Population analysis of plane-wave electronic structure calculations of bulk materials. *Phys. Rev. B* **54**, 16317–16320 (1996).

53. F. Shimojo, A. Nakano, R. K. Kalia, P. Vashishta, Electronic processes in fast thermite chemical reactions: A first-principles molecular dynamics study. *Phys. Rev. E* **77**, 066103 (2008).

54. O. F. Sankey, D. J. Niklewski, Ab initio multicenter tight-binding model for molecular-dynamics simulations and other applications in covalent systems. *Phys. Rev. B* **40**, 3979–3995 (1989).

55. J. M. Soler, E. Artacho, J. D. Gale, A. García, J. Junquera, P. Ordejón, D. Sánchez-Portal, The SIESTA method for ab initio order-N materials simulation. *J. Phys. Condens. Matter* **14**, 2745–2779 (2002).